small structures
www.small-structures.com

Engineering Nanoscale Homo–Heterojunction for Robust Z-Scheme CO_2 Conversion through Synchronous Amalgamation of Oxygen-Defective Ultrathin $BiVO_4$ and Red/Black Phosphorus

*Cheng-May Fung, Boon-Junn Ng, Chen-Chen Er, Wei-Kean Chong, Jingxiang Low, Xuecheng Guo, Xin Ying Kong, Hing Wah Lee, Lling-Lling Tan, Abdul Rahman Mohamed, and Siang-Piao Chai**

Sunlight-driven CO_2 conversion into value-added fuels emerges as an avant-garde strategy to mitigate the imminent energy scarcity and global warming. Nevertheless, sluggish charge kinetics and rapid carrier recombination are deemed as the foremost bottlenecks of efficient CO_2 photoreduction. In this contribution, the aforementioned shortcomings are addressed by assembling a homo–hetero architecture comprising oxygen-defective ultrathin $BiVO_4$ ($BiVO_4$–Ov) and red/black phosphorus (RP/BP) homojunction with a built-in nanoscale dual Z-scheme electronic configuration. The development of $BiVO_4$–Ov@RP/BP confers two electron relaying channels, that is, one from the RP/BP homojunction and another from the $BiVO_4$–Ov/RP heterojunction, which warrant the efficient separation of electron–hole pairs. Besides, the ultrathin 2D and oxygen vacant nature of $BiVO_4$–Ov exposes more active sites and renders electron trapping for efficient utilization of photogenerated charges. Amalgamating the desirable properties, the meticulously developed dual Z-scheme homo–heterojunction system on the basis of surface defect-engineered ultrathin $BiVO_4$–Ov nanosheets integrated with RP/BP offers a new avenue for the exploration, design, and fabrication of new generation photocatalysts with exceptional photocatalytic activities. In particular, the $BiVO_4$–Ov@RP/BP system demonstrates a remarkably high CH_4 yield of 14.52 μmol g^{-1} after 6 h of visible light illumination, which resembles a leading-edge photocatalytic performance among the existing $BiVO_4$- and P-based semiconductors.

1. Introduction

The fossil fuel energy system presents itself as the lifeblood of the modern economy as it powered the industrial revolution, lifted millions of people out of poverty, and molded today's cutting-edge society. The astronomical reliance on fossil fuels has not only inflicted worrisome energy crisis and fuelled global turmoil, their consumption also releases an abundance of anthropogenic greenhouse gases (GHGs), primarily carbon dioxide (CO_2). Since the industrial revolution in year 1750, the level of atmospheric CO_2 has reached a staggering concentration of 421 ppm in year 2022,[1] with its relentless increase being acknowledged as the dominant reason underlying the GHG effects and other associated environmental concerns, such as the El Niño phenomenon, the intensification of hurricanes and floods, as well as the reduction of marine plankton calcification.[2] The benefits of consuming fossil fuels are therefore accompanied with devastating downsides. One of the greatest responsibilities facing humanity today is to mitigate CO_2-induced global warming and climate

C.-M. Fung, B.-J. Ng, C.-C. Er, W.-K. Chong, L.-L. Tan, S.-P. Chai
Multidisciplinary Platform of Advanced Engineering
Chemical Engineering Discipline, School of Engineering
Monash University Malaysia
Selangor 47500, Malaysia
E-mail: chai.siang.piao@monash.edu

The ORCID identification number(s) for the author(s) of this article can be found under https://doi.org/10.1002/sstr.202300083.

DOI: 10.1002/sstr.202300083

J. Low, X. Guo
Hefei National Laboratory for Physical Sciences at the Microscale
University of Science and Technology of China
Hefei, Anhui 230029, P. R. China

X. Y. Kong
School of Chemistry, Chemical Engineering and Biotechnology
Nanyang Technological University
637371 Singapore, Singapore

H. W. Lee
Center for Semiconductor & Thin Film Research
MIMOS Berhad
Kuala Lumpur 57000, Malaysia

change and the core to all climate change solutions is to decrease the dependence on fossil fuel as well as minimize GHG emissions. The transformation of CO_2 into chemical building blocks and value-added fuels is garnering incessant attention ascribing to the growing sense of urgency to design, develop, and implement a carbon-neutral and sustainable economy.

The Earth receives plenty of solar energy for the society's modern energy-intensive lives. Hence, direct solar-to-fuel transformation via the photocatalysis technology accords a major advance in this direction as it harvests the inexhaustible, safe, and clean energy of the Sun in a nonhazardous, sustainable, and economically viable manner to convert CO_2 into fuels like methane (CH_4), formic acid (CH_2O_2), and methanol (CH_3OH).[3] Despite years of devotion in the research of CO_2 photocatalysis, CO_2 conversion performance is still wide of the target from meeting satisfactory industry requirement, which generally stems from aspects such as the intrinsic limitations of semiconductor photocatalysts and the thermodynamically stable electron configuration of the CO_2 molecules with linear symmetry. Traditional photocatalysts suffer from poor separation of charge carriers and inadequate surface active sites, resulting in inferior photocatalytic performances. This phenomenon is further exacerbated by the high overpotential needed to activate CO_2 molecules, which remains arduous for many photocatalytic materials.[4] To realize CO_2 transformation practically, the present research wave is steered by the construction of 2D structures that are exceptional for building efficient photocatalytic materials due to their distinctive 2D geometry, electronic anisotropy, enriched surface active sites, expanded surface area, reduced charge transportation routes, and improved conductivity owing to the increased surface defects.[5] The synergistic exploitation and optimization of 2D photocatalysts could impart outstanding activities in comparison to their bulk and 3D counterparts. Specifically, the advantages of a 2D photocatalyst are closely associated with three main aspects: 1) expanded specific surface area which proffers an increased density of highly-exposed active centers; 2) reduced transfer routes for the migration of photogenerated electron–hole pairs to the surface of the photocatalyst to participate in redox reactions; and 3) enhanced mechanical properties such as improved durability, especially when 2D structures are hybridized with other photocatalysts.[6] Moreover, 2D materials with ultrathin geometry proffer the opportunity to engineer and tune their electronic structures beyond the bulk realm, attributing to the obvious distinctions in local atomic structures.[7] The recent progress in 2D materials has therefore sparked a surge of interest in exploring metal oxide–based materials. Specifically, bismuth vanadate ($BiVO_4$), an n-type semiconductor offers vast potential in the photocatalysis scene as it is endowed with high photo- and chemical stability, nontoxic nature, low production cost, and a narrow bandgap of ≈2.4 eV with flexible optoelectronic features. The visible-light responsiveness of $BiVO_4$ renders it as a competitive candidate to harvest light energy from the solar spectrum. More importantly, $BiVO_4$ photocatalyst is spectacularly bestowed with a strong valence band (VB) potential of ≈2.7 V (vs. NHE), making it a befitting option to serve as a powerful oxidation counterpart for CO_2-reduction process.[8]

To modulate and further enhance the physicochemical characteristics and catalytic capabilities of $BiVO_4$, immense emphasis has been placed on defect engineering with a particular focus on the introduction of oxygen vacancies in $BiVO_4$ as the implementation of oxygen vacancies has been proven not only to improve the optical absorption properties of metal oxides but also to propitiously modulate the electronic characteristics of photocatalysts and suppress the rapid recombination of charge carriers.[9–11] Typically, an oxygen vacancy is created when an oxygen atom escapes from the lattice of a metal oxide, resulting in enhancement of visible-light absorption attributed to the creation of isolated level below conduction band (CB) as well as ameliorating electrical conductivity.[12] The enhancement in optical properties and charge-carrier dynamics generally stems from the alteration of the intrinsic electronic properties and bandgap of the photocatalytic material upon the introduction of oxygen vacancy into its lattice structure as the modification allows the generation of local energy defect levels below CB. As such, the introduction of oxygen vacancies has been demonstrated to improve a myriad of photocatalytic reactions[13–15] by virtue of these defect states serving as trapping points which lead to the suppression of exciton recombination process. Further survey reveals the ability of oxygen-vacancy defects to enrich the surface properties of $BiVO_4$ (water [H_2O] adsorption sites and active reaction sites) in substrate binding for efficacious photocatalysis.[16]

In recent years, elemental red phosphorus (RP) has been arousing extensive interests for multitudinous photocatalytic applications ascribed to its abundant availability, broad visible-light responsivity, high stability, nontoxic, and low-cost nature.[17] Considerable efforts have been devoted to developing RP as a functional material for photocatalytic CO_2 reduction with fascinating structural and optoelectronic properties. However, the photocatalytic potential of RP is restricted owing to the poor separation and transfer of electrons and holes due to charge-trapping centers being present on the semiconductor's surface. Therefore, continuous efforts toward engineering high-performing RP-based materials and modification strategies are the cruces in surmounting the limitations of RP. Hitherto, the fabrication of RP-based photocatalysts namely the preparation of nanostructured and/or crystalline RP, heterojunction construction, and cocatalyst loading to name a few is soaring within the research community. Among the strategies employed, designing a transitional phase of *P*-based photocatalyst that comprises red–black phosphorus (RP/BP) homojunction accords a desirable feat to curb the drawbacks of pure RP.[18] This is because the black counterpart possesses a tunable bandgap across a wide region, from a bulk value of 0.3 eV to a value of 2.0 eV for the monolayer structure, rendering its strong optical absorption in the visible and near-infrared (NIR) spectrum. BP's astounding charge-carrier mobility ($\approx 10^2$–$\approx 10^4$ $cm^2 V^{-1} s^{-1}$) makes the topotactic transformation of RP to BP to form a mixed-phase homojunction photocatalyst immensely attractive. Moreover, the development of the transitional phase RP/BP photocatalysts is ascertained to

A. R. Mohamed
School of Chemical Engineering
Universiti Sains Malaysia
Nibong Tebal 14300, Pulau Pinang, Malaysia

augment the light responsivity of bare RP photocatalyst, as evidenced by the powerful optical absorption properties of BP which extends up to the NIR region. In light of the intriguing physicochemical and semiconducting properties displayed by RP and BP, respectively, the development of RP/BP homojunction photocatalysts are highly propitious to heighten the efficiency of photocatalytic CO_2 reduction.

With that in mind, the opportune construction of an effective dual Z-scheme homo–heterojunction system ($BiVO_4$–Ov@RP/BP) via the cooperative combination of oxygen-defective ultrathin 2D $BiVO_4$ ($BiVO_4$–Ov) and a phosphorus (P)-based homojunction photocatalyst comprising RP/BP can provoke complementary synergism in accomplishing remarkable CO_2-photoreduction performance. Attributing to the difference in Fermi levels between the semiconductors, depletion layers are generated at the interface of $BiVO_4$–Ov and RP/BP homojunction, leading to the accelerated directional migration of electron–hole pairs powered by the built-in electric field. Working synergistically with the oxygen vacancies throughout the ultrathin 2D $BiVO_4$ nanosheets, the $BiVO_4$–Ov@RP/BP composite photocatalytic system demonstrated an exceptional CH_4 yield of $14.52\,\mu mol\,g^{-1}$ under visible-light irradiation. Merging all the aforementioned merits, we believe that this pioneering study will provide compelling insights into the significance of combining ultrathin 2D material design, defect engineering, and dual Z-scheme vectorial charge transfer to regulate nanoscale-level charge steering and modulate the density of surface active centers to promote superior photoreduction of CO_2.

2. Results and Discussion

2.1. Morphology and Structural Characterization

X-Ray diffraction (XRD) was first utilized to assess the phase structure of the samples and the results are depicted in **Figure 1**a. As can be seen from the figure, the XRD diffraction peaks of $BiVO_4$–Ov at $2\theta = 19.0°$, 28.9°, 30.5°, 34.5°, 39.8°, 42.5°, 50.3°, and 53.2° correspond to the (110), (−121), (040), (200), (211), (051), (202), and (−161) planes of monoclinic scheelite type $BiVO_4$ (JCPDS No. 00-014-0688), respectively. The exposure of the (040) crystal plane is immensely conducive for higher photocatalytic oxidation reactions. Typically, active catalytic centers are located in the edge sites of metal oxides whereas the basal planes remain catalytically inert which restricts photocatalytic activity.[19] The introduction of oxygen-vacancy defects as well as the ultrathin dimension of the as-developed $BiVO_4$–Ov nanosheets result in the activation of basal planes through the exposure of more catalytic reactive centers, thereby improving photocatalytic capacity. The (040) peak also reveals the orientation of the monoclinic $BiVO_4$–Ov along the [010] zone axis.[20] Moreover, preceding research have disclosed that the photoinduced charge carriers in monoclinic $BiVO_4$ would preferentially travel to {010} and {110} facets ascribed to the distinctive band energies between the two, thereby accelerating the separation of electrons and holes.[21] In contrast, the RP/BP homojunction exhibits the XRD patterns of pure BP (JCPDS card no. 01-076-1967) as BP is highly crystalline in nature while RP possesses amorphous

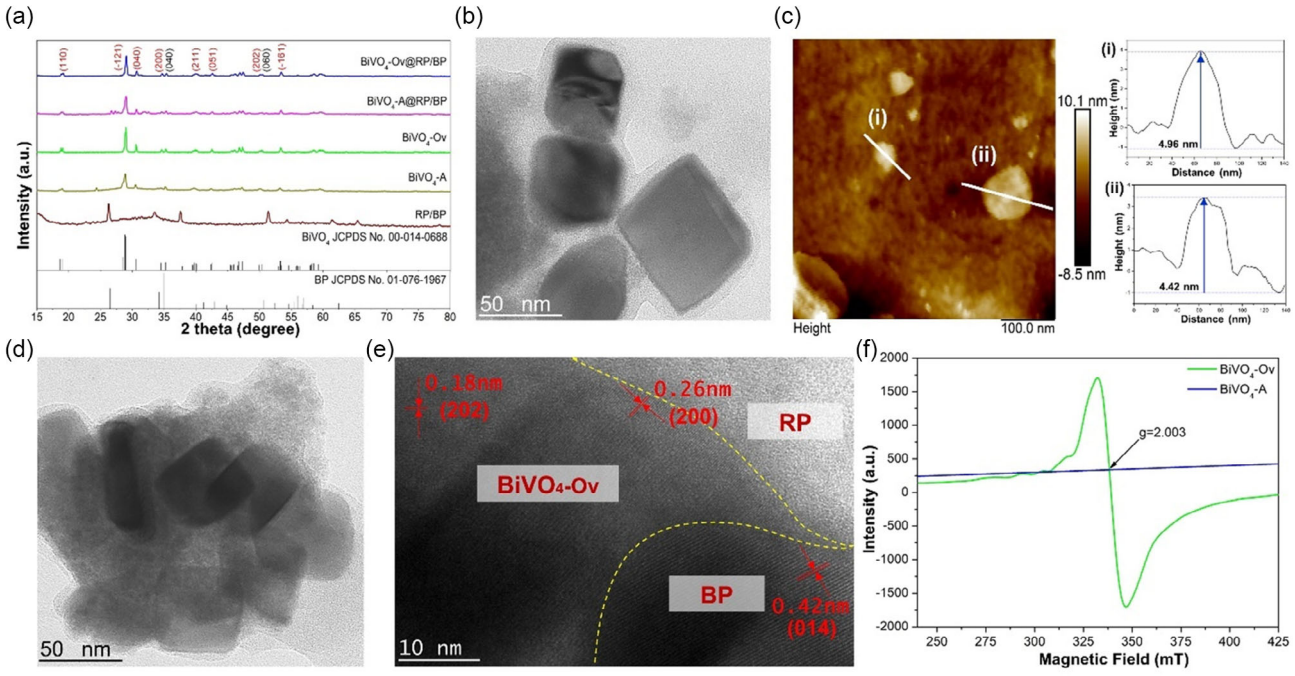

Figure 1. a) X-Ray diffraction (XRD) spectra of RP/BP, $BiVO_4$–A, $BiVO_4$–Ov, $BiVO_4$–A@RP/BP, and $BiVO_4$–Ov@RP/BP photocatalysts. Crystal planes of $BiVO_4$ and BP are indicated by the red and black indexes, respectively. b) Transmission electron microscopy (TEM) image of ultrathin $BiVO_4$–Ov nanosheets. c) Atomic force microscopy (AFM) image and the corresponding height profiles of ultrathin $BiVO_4$–Ov nanosheets. d) TEM and e) high-resolution TEM (HRTEM) images of $BiVO_4$–Ov@RP/BP composite photocatalyst. f) Electron spin resonance (ESR) spectra of $BiVO_4$–Ov photocatalysts before (green line) and after (blue line) annealing.

characteristics. That said RP/BP demonstrates XRD peaks at $2\theta = 26.30°$, 35.20°, and 50.40°, which are well indexed to the (021), (040), and (060) planes of pure orthorhombic BP, respectively. Typical descriptive diffraction patterns of both $BiVO_4$ and mixed-phase RP/BP are present in the $BiVO_4$–A@RP/BP and $BiVO_4$–Ov@RP/BP composite photocatalysts.

The morphology, microstructure, and topography of the developed samples were then assessed using field-emission scanning electron microscope (FESEM), atomic force microscopy (AFM), transmission electron microscopy (TEM), and high-resolution TEM (HRTEM). From the FESEM image displayed in Figure S1a, Supporting Information, a porous morphology is clearly discerned for the RP/BP sample whereas TEM image featured in Figure 1b reveals the as-synthesized $BiVO_4$–Ov as 2D nanosheets that possess quasi-square-sheet shapes with average lateral sizes ranging from 50 to 100 nm. To garner an overview of the thickness of $BiVO_4$–Ov nanosheets, AFM was employed and the topography image with the corresponding height profiles are shown in Figure 1c. Based on the image, it can be evidently seen that $BiVO_4$–Ov possesses an average thickness of 4 to 5 nm, corroborating its ultrathin nature. In stark comparison to the conventional irregular rod-like structure of bulk $BiVO_4$ ($BiVO_4$–B) (Figure S1b, Supporting Information), $BiVO_4$–Ov presents itself as a square-like ultrathin structure with less obvious bulk domains. The elemental composition of $BiVO_4$–Ov@RP/BP was divulged using FESEM energy-dispersive X-Ray spectroscopy (FESEM-EDX) mapping (Figure S1c,d, Supporting Information), which show the homogeneous distribution of P, Bi, V, and O elements, affirming the successful hybridization between $BiVO_4$–Ov and RP/BP. The successful construction of a $BiVO_4$–Ov@RP/BP hybrid photocatalytic system is further verified by TEM imaging (Figure 1d). It can be visualized that $BiVO_4$–Ov with a square-like geometry is successfully composited onto RP/BP with intimate contact. The examination of crystallographic structure and lattice fringe spacing measurements for the composite photocatalyst was subsequently undertaken using HRTEM (Figure 1e). Two interplanar d-spacings of 0.18 and 0.26 nm are attained from the HRTEM analysis, which could be indexed to the (202) and (200) crystallographic planes of monoclinic $BiVO_4$–Ov, respectively.[22] These findings are in good agreement with the XRD analysis. The d-spacing of 0.42 nm, in contrast, corresponds to the (014) plane of the BP crystals.[23,24] The region which displays undistinctive lattice spacings with poor crystallinity (labeled with RP from inset of Figure 1e) is indicative of the amorphous nature of the RP allotrope. The coexistence of the lattice spacings of $BiVO_4$–Ov, BP, and amorphous RP further affirms the propitious amalgamation of the three semiconductors to craft a $BiVO_4$–Ov@RP/BP homo–heterojunction.

To verify the presence of oxygen vacancies, the $BiVO_4$–Ov nanosheets were annealed in air at 500 °C to eliminate oxygen-vacancy defects and the validation was conducted by electron spin resonance (ESR). As one of the most efficacious methods to probe defective structures, ESR analysis evinces a symmetrical resonance line centered at $g = 2.003$ as can be seen from Figure 1f for the $BiVO_4$–Ov sample due to the accumulation of electrons on the oxygen-vacancy defects.[25] As anticipated, no ESR signal was detected for the annealed sample ($BiVO_4$–A). In monoclinic $BiVO_4$, ESR signals are not contributed by both high (Bi^{3+} and V^{5+}) and low valent ions (Bi^{+}, V^{3+}, and O^{2-}), owing to the absence of unpaired electrons. Similarly, the ESR signal would not be caused by the oxygen vacancy that is doubly positively charged (V_o^{2+}) as there is no diamagnetic electron. Therefore, the distinct ESR signal would be sourced from the oxygen vacancy that is singly negatively charged ($V_o^{\cdot}$) in which the trap-free electron is provided by V^{4+} and/or Bi^{2+}.[26] A dramatic decrease of the ESR signal is witnessed for the $BiVO_4$–A sample, suggesting the elimination of oxygen vacancies throughout the 2D $BiVO_4$ nanosheets upon the introduction of atmospheric oxygen.

To expound the elemental composition and chemical valency of the samples, X-Ray photoelectron spectroscopy (XPS) analysis was undertaken. The complete XPS survey spectra of $BiVO_4$–Ov@RP/BP reveal the presence of P, Bi, V, and O as the main elements as evidenced from Figure S2, Supporting Information. In accordance with **Figure 2**a which unveils the P 2p spectra of the RP/BP sample, two narrow peaks were observed at 130.42 and 131.29 eV, which corresponds to elemental P $2p_{3/2}$ and P $2p_{1/2}$ of the P–P bonds, respectively. In contrast, a broader and wider sub-band can be found at 135.02 eV, suggesting that oxidized P species (P_xO_y) is present.[27] Contrastingly, the P $2p_{3/2}$ and $2p_{1/2}$ characteristic peaks of the $BiVO_4$–Ov@RP/BP sample located at 129.78 and 130.65 eV experience diminished intensities with the formation of two new peaks situated at 133.18 and 134.25 eV, attributing to the generation of O–P=O and P–O, respectively.[28,29] Notably, the P $2p_{3/2}$ and $2p_{1/2}$ XPS peaks for $BiVO_4$–Ov@RP/BP are shifted toward lower binding energies with a difference of 0.64 eV in comparison to the RP/BP sample. Conversely, deconvolution of the Bi 4f spectra (Figure 2b) for the bare $BiVO_4$–Ov sample features a classic spin–orbit doublet splitting centered at 159.20 and 164.50 eV with a difference of 5.30 eV, implying the presence of the Bi^{3+} species whereas the V 2p spectra (Figure 2c) illustrates two characteristic peaks at 516.73 and 524.26 eV with a peak splitting of 7.53 eV, which represents V^{5+}.[30,31] As opposed to bare $BiVO_4$–Ov, the Bi 4f and V 2p characteristic peaks for the $BiVO_4$–Ov@RP/BP composite photocatalyst experience an increment in binding energies, indicating the change in the chemical environment upon the integration with RP/BP. Interestingly, the positive shift in binding energies of the Bi 4f and V 2p spectra accompanied by the negative shift in binding energies of the P 2p spectra suggest the intimate interfacial contact and electronic coupling between $BiVO_4$–Ov and P-based photocatalysts. In contrast, the asymmetric O 1s spectra for the $BiVO_4$–Ov sample as illustrated in Figure 2d are deconvoluted into three peaks centered at 530.60, 531.40, and 532.60 eV, which reflects the lattice oxygen (O_L), deficient oxygen (O_V), and chemisorbed oxygen (O_C), respectively.[25,26,32] Accordingly, a notable amount of oxygen vacancies can be detected in the as-developed ultrathin $BiVO_4$–Ov nanosheets. As for the hybrid photocatalyst, the O 1s spectra discloses three peaks situated at 530.55, 531.27, and 532.14 eV, which arise from the lattice O^{2-} atoms, Ov, and P–O–P, respectively.[33,34] Based on the XPS analysis, the shift in binding energies provides direct evidence for the successful formation of $BiVO_4$–Ov@RP/BP homo–heterojunction with interfacial depletion layer that resembles the cascade flow of electrons.[35]

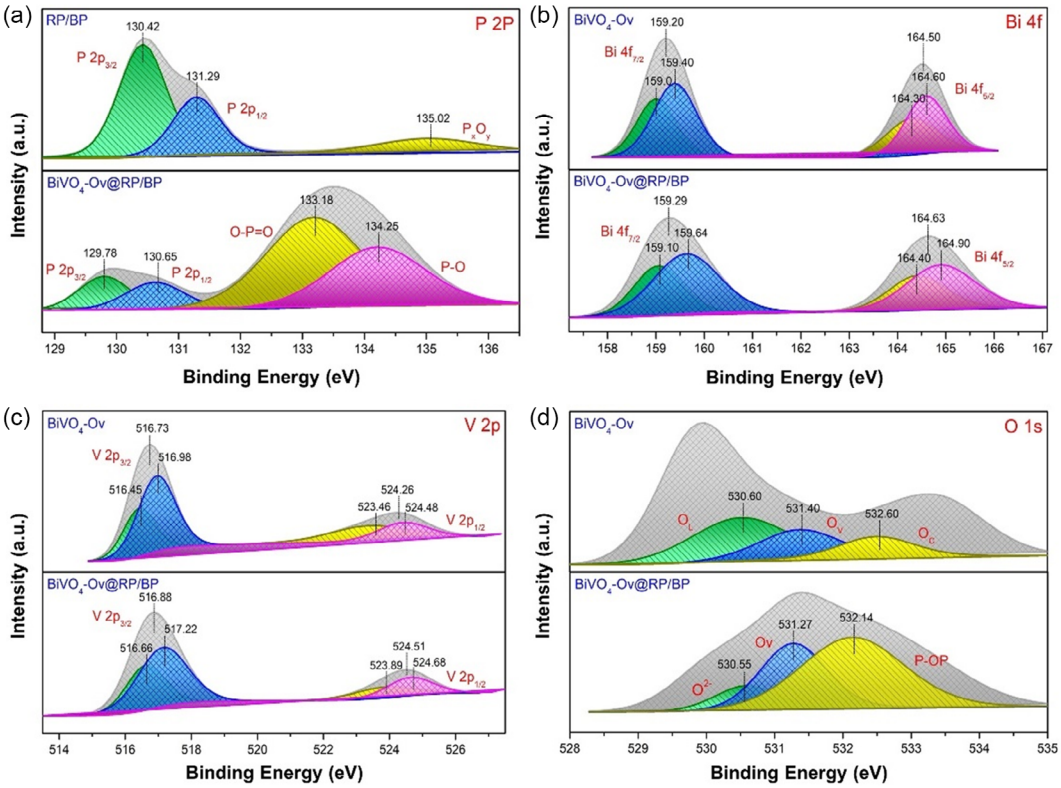

Figure 2. X-Ray photoelectron spectroscopy (XPS) spectra of mixed-phase RP/BP homojunction, $BiVO_4$–Ov nanosheets and $BiVO_4$–Ov@RP/BP composite photocatalysts: a) P 2p scan, b) Bi 4f scan, c) V 2p scan, and d) O 1 s scan.

2.2. Optoelectronic Properties and Charge-Transfer Mechanisms

The insights on the light-harvesting kinetics of the as-prepared samples were assessed via ultraviolet-visible diffuse reflectance spectroscopy (UV–Vis DRS) as demonstrated in **Figure 3**a. The topotactic conversion of RP to mixed-phase RP/BP homojunction witnesses the enhancement of the absorption edge of RP to the NIR region due to the presence of BP with broadband absorption in the UV to NIR region. Specifically, the absorption edge of RP/BP sample is observed at 760 nm with an extension to the spectral range beyond 800 nm while exhibiting NIR absorption tail. On another note, the absorption edge of $BiVO_4$–Ov is discerned at 530 nm with the display of a much more intense visible-light absorption capacity as opposed to the $BiVO_4$–A counterpart. Additionally, the long absorption tail of $BiVO_4$–Ov presents indisputable corroboration for the existence of large amount of surface defects throughout the sample such that the band tails of the defect states can be determined from the Urbach rule which is expressed by Equation (1).[36]

$$\alpha = \alpha_0 \ \exp\left(\frac{\mathrm{hv}}{\mathrm{Eu}}\right) \tag{1}$$

α resembles the absorption coefficient whereas α_0 denotes a constant. The photon energy of the incident light is represented by hv, and the Urbach energy which is also the energy of the band tail is represented by Eu. By presuming the inverse gradient of the plot of ln α vs. hv as shown in Figure S3, Supporting Information, correlation between the energy of transition between the defect state and CB edge can be made using the Urbach energy. The Eu value was subsequently determined to be 0.18 eV, signifying the gap between the CB edge and the oxygen-vacancy-induced defect state. Evidently, it can be affirmed that the defect states are judiciously positioned below the CB. In addition, a redshift in the absorption edge of the $BiVO_4$–Ov sample is identified, reflecting the narrowing of bandgap. In addition, the hybrid photocatalysts were found to be photoresponsive over a broad spectrum of solar energy. Further investigation unveils the formation of two absorption shoulders, as manifested in both $BiVO_4$–Ov@RP/BP and $BiVO_4$–A@RP/BP. In detail, the $BiVO_4$ photocatalysts contribute to the shoulder that is located at an absorption edge of 580 nm whereas the integration of RP/BP gives rise to the absorption edge beyond 600 nm; thus, this phenomenon validates the intimate contact between $BiVO_4$–Ov and RP/BP. Integrating the favorable features of both RP/BP and $BiVO_4$–Ov, the photoresponsivity of $BiVO_4$–Ov@RP/BP covers a wide solar spectrum from the UV up to the NIR region, implying the capability of the composite system to generate greater number of charge carriers for participation in photocatalytic reactions, resulting in improved performance. In accordance with the transformed Kubelka–Munk (KM) plots as delineated in Figure S4a,b, Supporting Information, the bandgap values of RP/BP and $BiVO_4$–Ov were found to be 1.80 and

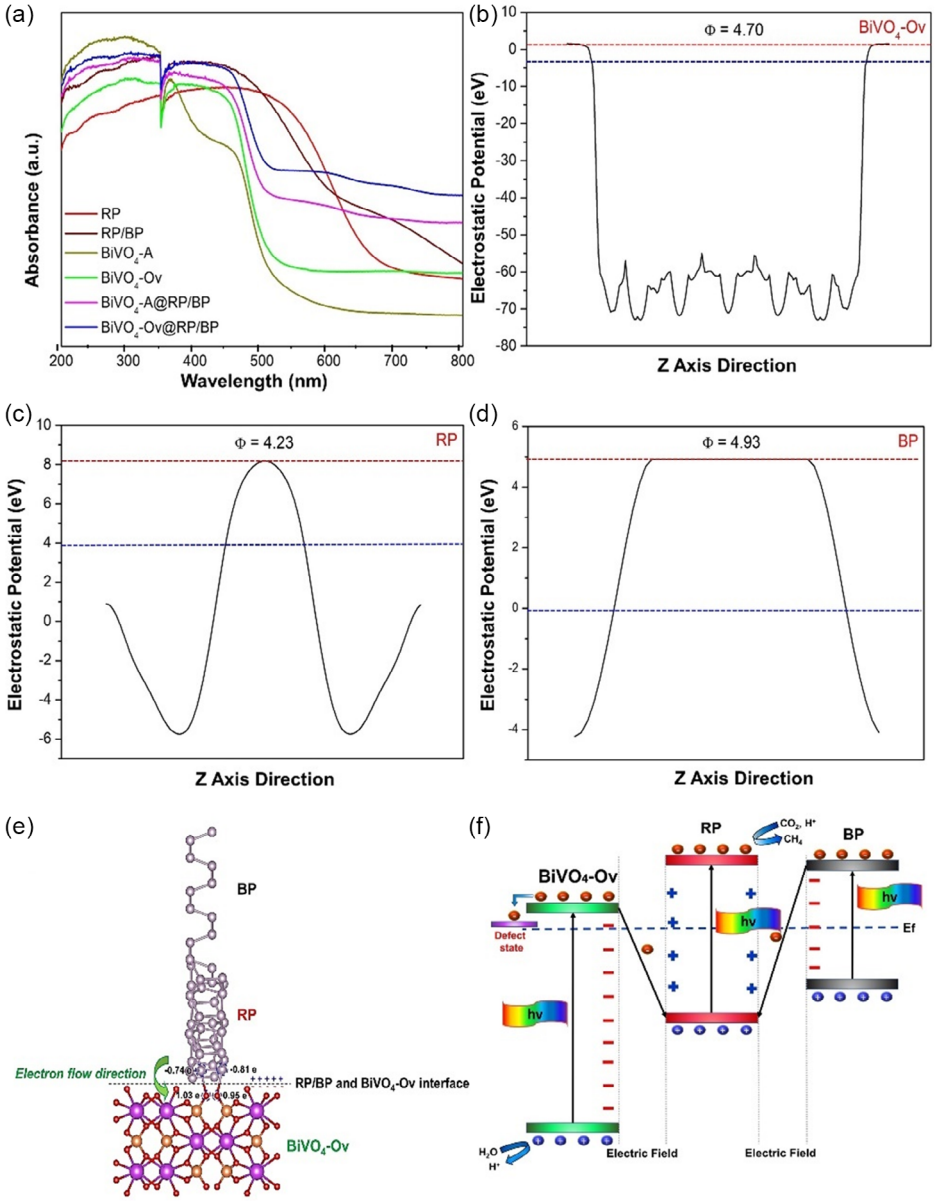

Figure 3. a) UV–Vis diffuse reflectance spectroscopy (UV–Vis DRS) spectra of RP, RP/BP, $BiVO_4$–A, $BiVO_4$–Ov, $BiVO_4$–A@RP/BP, and $BiVO_4$–Ov@RP/BP photocatalysts. Work function of b) $BiVO_4$–Ov, c) RP, and d) BP obtained using first principles calculations. e) Bader charge analysis on the $BiVO_4$–Ov@RP/BP model to deduce interfacial charge transfer via the Z-scheme pathway. f) Charge transportation mechanism at the dual Z-scheme homo–heterointerface in the $BiVO_4$–Ov@RP/BP composite photocatalyst.

2.56 eV, respectively. To investigate the electronic structure of RP/BP and $BiVO_4$–Ov as well as to glean mechanistic insights into the plausible charge-transfer pathway within the composite system, Mott–Schottky analysis was conducted as it provides critical information regarding the flat-band potential (E_{FB}) of the samples. Accordingly, the E_{FB} of RP/BP was measured to be −1.04 V via the extrapolation of the Mott–Schottky plot (Figure S4c, Supporting Information) whereas $BiVO_4$–Ov possesses an E_{FB} of 0.01 V (Figure S4d, Supporting Information). The display of an apparent upward slope for both photocatalysts based on the Mott–Schottky graphs is consistent with the n-type behavior of semiconductors, and as a rule of thumb, the CB potential of n-type material is 0.20 V more negative than the E_{FB}. With that in mind, the CB position of RP/BP and $BiVO_4$ were then predicted to be −1.24 and −0.19 V (vs. Ag/AgCl). Since the conversion of E_{FB} with respect to NHE obeys the relationship $V_{NHE} = V_{Ag/AgCl} + 0.197$ V,[37] the CB potential of RP/BP was calculated to be −1.04 V whereas its VB potential was proposed to be 0.76 V (vs. NHE). By adopting a similar approach, the CB and VB potentials of $BiVO_4$–Ov were found to be 0.01 V (vs. NHE) and 2.55 V (vs. NHE), respectively.

In accordance with the bandgap values, CB and VB potentials attained for $BiVO_4$–Ov and RP/BP, dual Z-scheme mechanism and double-charge transportation are two probable routes

involved in the photocatalytic reduction of CO_2 using RP/BP@$BiVO_4$–Ov. First, in the dual Z-scheme system, by the recombination of CB electrons of BP and $BiVO_4$–Ov with the VB holes of RP, the transfer of photoinduced electrons in the CB of RP to the CB of both BP and $BiVO_4$–Ov is brought to a halt, which is beneficial for the spatial isolation of electrons in the CB of RP and holes in the VB of BP and $BiVO_4$. Thus, the dual Z-scheme mechanism preserves the strong reduction and oxidation capacity of the photocatalyst owing to the seamless separation and maintenance of electrons and holes in the CB and VB, respectively.[38] To corroborate this claim, the Fermi energy level and work function of each component were studied using first principles calculations. According to density-functional theory (DFT) calculations (Figure 3b–d), the work functions of $BiVO_4$–Ov, RP, and BP were determined to be 4.70, 4.23, and 4.93 eV, respectively. The work function values attained from DFT calculations are further ratified using ultraviolet photoelectron spectroscopy (UPS) analysis with He I as the excitation source. As depicted in Figure S5, Supporting Information, the secondary cutoff binding energy (E_{Cutoff}) of RP/BP and $BiVO_4$–Ov were determined to be 17.64 and 17.31 eV, respectively, via the extrapolation of the linear region to the base line of the UPS spectra. By using the formula $\Phi = h\nu - E_{Cutoff}$, the work function (Φ) of RP/BP and $BiVO_4$–Ov were calculated to be 4.36 and 4.69 eV, respectively, which is in good agreement with the work function values acquired using DFT calculations. Bader charge analysis was undertaken via DFT calculations to elucidate the transportation of charges and further substantiate the formation of Z-scheme at the $BiVO_4$@RP/BP interface. In accordance with the Bader analysis, a positively charged atom typically resembles an electron-rich atom whereas a negatively charged atom implies a deficiency of electrons. In accordance with Figure 3e, the negatively charged P atoms (−0.74 and −0.81 e) indicate depletion of electrons while the positively charged atoms of $BiVO_4$–Ov (1.03 and 0.95 e) indicate accumulation of electrons. Hence, it can be deduced that free electrons were transferred from RP to $BiVO_4$–Ov during the equilibration of Fermi levels. Working in unison with the bandgap values attained from the transformed KM plots, the respective electronic band structure of $BiVO_4$–Ov, RP and BP is proposed as can be seen in Figure S6, Supporting Information. When all three components are in contact, the free electrons from RP possessing higher Fermi energy level diffuse into $BiVO_4$–Ov and BP due to the imbalance in concentration of charges as a result of the difference in Fermi energy levels. Following the diffusion of charges at the interface of $BiVO_4$–Ov/RP and RP/BP, the energy band of RP experiences a concomitant downward shift while the Fermi energy levels of $BiVO_4$–Ov and BP shift upward until an equilibration in Fermi energy level is reached. This occurrence results in the generation of depletion layers at the interfaces of the homo–heterostructure as the interface of RP amasses positive charges while the interfaces of $BiVO_4$–Ov and BP accumulate negative charges. The formation of two space-charged regions, also referred to as the dual Z-scheme homo–heterojunction, can create internal electric fields and Coulomb interactions near the interface of $BiVO_4$–Ov/RP and RP/BP, which represents Ohmic contact for vectorial transfer of electrons. This powers the accelerated separation and migration of charge carriers which in turn depresses the recombination of electron and holes while maintaining strong redox performance. A clearer insight into the plausible charge transportation pathway of the nanocomposite is portrayed in Figure 3f. The rate of CH_4 production is further enhanced as more reductive electrons and oxidative holes are formed in the CB and VB of RP and $BiVO_4$, respectively. This is because a more negative redox potential of −1.04 V (vs. NHE) is proffered for the reduction of CO_2 to CH_4. Similarly, more oxidative holes are formed in the VB of $BiVO_4$–Ov for H_2O oxidation. In other words, the dual Z-scheme mode propounds a much more superior reduction and oxidation potential for photocatalytic surface redox reactions accompanied by the improved separation, migration, and isolation of electron–hole pairs. That said, the dual Z-scheme system is highly likely to be generated. It is worth noting that the surface vacancy defects present throughout $BiVO_4$–Ov nanosheets could act as potent electron-trapping centers to hinder electron–hole pairs recombination by extending the lifespan of photoexcited charges. The integration of dual Z-scheme mechanism with defect engineering via the formation of oxygen vacancies could govern the efficient photoreduction performance of $BiVO_4$–Ov@RP/BP.

Contrastingly, double-charge migration indicates the transfer of electrons from the CB of RP to the CB of BP and $BiVO_4$–Ov (Figure S7, Supporting Information). On top of that, the double-charge-transfer mechanism features the transportation of photogenerated holes in the VB of BP and $BiVO_4$–Ov to the VB of RP. Despite the adequate electron–hole separation induced by the double-charge-transfer mode, such a homo–heterojunction system reduces the redox capability of light-excited charge carriers. On the one hand, a minimum redox potential of 0.82 V (vs. NHE) is essential for the photooxidation of H_2O. Nevertheless, the oxidation potential of VB in RP (0.76 V vs. NHE) is less positive than 0.82 V. Hence, the double-charge-transfer system deprives the photogenerated holes of engaging in the oxidation of H_2O. On the other hand, the CBM of $BiVO_4$–Ov (0.01 V vs. NHE) is less negative than the redox potential required for the generation of CH_4 (−0.24 V vs. NHE), thereby diminishing the driving force of CO_2 transformation into CH_4. Consequently, the domination of the double-charge-transfer mechanism to justify the photocatalytic reduction of CO_2 over RP/BP@$BiVO_4$–Ov is implausible.

2.3. Photoreduction of CO_2 and Mechanisms for Improved Performance

To examine the photocatalytic performances of the as-developed samples, visible-light-powered gas-phase CO_2 reduction was undertaken at ambient conditions. The total CH_4 yield generation over the photocatalysts is rendered in **Figure 4**a. As envisaged, $BiVO_4$–Ov@RP/BP manifested the highest CH_4 yield of 14.52 μmol g^{-1} while negligible CH_4 production was detected for the solitary RP/BP, $BiVO_4$–A, and $BiVO_4$–Ov samples. The maximum CH_4 generation exhibited by the $BiVO_4$–Ov@RP/BP composite provides direct evidence on the importance of Z-scheme homo–heterojunction formation as the coupling between $BiVO_4$–Ov, which possesses powerful oxidation capacity and RP/BP with high reduction potential complements one another seamlessly by demonstrating a stark enhancement in photoactivity. To consolidate the pivotal role of oxygen-vacancy defects in ameliorating photocatalytic CO_2-reduction reactions,

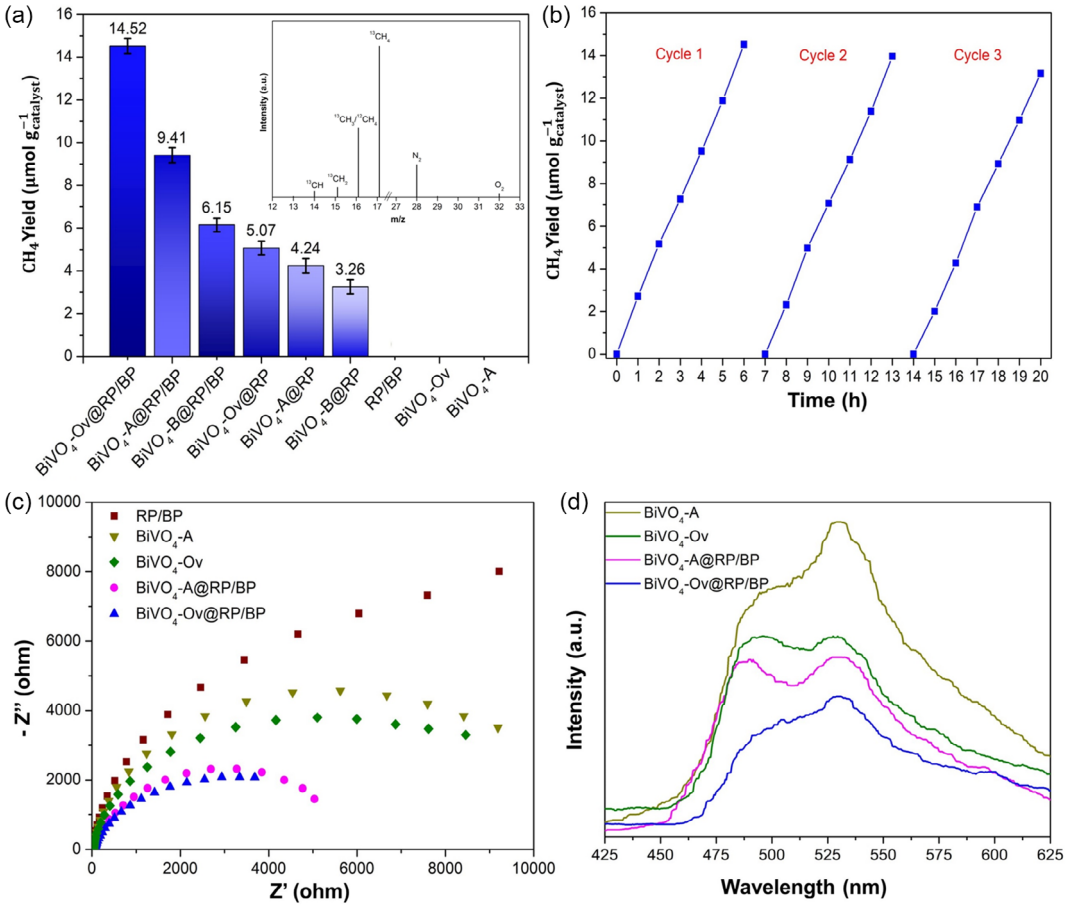

Figure 4. a) Total photocatalytic CH_4 yield of $BiVO_4$–Ov@RP/BP, $BiVO_4$–A@RP/BP, $BiVO_4$–B@RP/BP, $BiVO_4$–Ov@RP, $BiVO_4$–A@RP, $BiVO_4$–B@RP, RP/BP, $BiVO_4$–Ov, and $BiVO_4$–A photocatalysts over 6 h of visible-light illumination; inset shows the gas chromatography mass spectrometry (GC–MS) chromatogram of $^{13}CH_4$ ($m/z = 17$) produced by $BiVO_4$–Ov@RP/BP in the photoreduction of $^{13}CO_2$. b) Cycling tests of CO_2 photoreduction over $BiVO_4$–Ov@RP/BP photocatalyst. c) Nyquist impedance plots and d) steady-state photoluminescence (PL) curves for RP/BP, $BiVO_4$–A, $BiVO_4$–Ov, $BiVO_4$–A@RP/BP, and $BiVO_4$–Ov@RP/BP photocatalysts.

comparisons between the CH_4 yield of $BiVO_4$–A@RP/BP and $BiVO_4$–Ov@RP/BP were made whereby the latter displayed a distinctive 1.5-fold improvement in photoactivity as opposed to $BiVO_4$–A@RP/BP (9.41 μmol g^{-1}) without oxygen vacancies. This phenomenon could be ascribed to the attraction of negative charge carriers to the vacancy centers as a result of the absence of oxygen atom from the $BiVO_4$ crystal lattice in the $BiVO_4$–Ov@RP/BP sample, leading to a higher density of local charge carriers. Consequently, fortified visible-light harvesting with intense tail absorption in the NIR region is induced as proven by the UV–Vis spectra (Figure 3a) due to bandgap narrowing of $BiVO_4$–Ov, this phenomenon is highly desirable as the strengthened light harvesting capability of $BiVO_4$–Ov is envisaged to increase the photogeneration of electron–hole pairs, which is conducive for photocatalytic reactions. Moreover, oxygen-vacancy defects and the generation of sub-bands in $BiVO_4$–Ov as featured in Figure 3f play indispensable roles in enhancing the separation of electron–hole pairs as an additional pathway is created for second-step electron transfer from the CB of $BiVO_4$–Ov to the local defect states in lieu of the direct transition of electrons between CB and VB. When photogenerated electrons subside back to the VB from the CB, the electrons could reside temporarily in the sub-bands prior to recombination with the VB holes. This mechanism ultimately improves the spatial separation of charge carriers as well as photocatalytic performance as the faster-moving holes are now available in abundance to participate in photocatalytic oxidation reactions. Additionally, the presence of surface oxygen vacancies also strengthens the interaction between $BiVO_4$–Ov and H_2O, facilitating charge transfer and decreasing the energy required to dissociate H_2O.[39]

On top of that, the importance of ultrathin 2D material design for semiconductors was also investigated through assessing the yield of $BiVO_4$–A@RP/BP with ultrathin 2D $BiVO_4$ nanosheets and $BiVO_4$–B@RP/BP with bulk $BiVO_4$. As discerned from Figure 4a, the CH_4 yield recorded for $BiVO_4$–A@RP/BP is an astounding 1.5-time enhancement in comparison to $BiVO_4$–B@RP/BP (6.15 μmol g^{-1}), corroborating the significance of ultrathin 2D material construction in elevating photocatalytic activities. Specifically, the ultrathin 2D $BiVO_4$ could improve exciton spatial separation and migration, molecule

adsorption, as well as the activation of photocatalytic processes owing to their thickness in the atomic scale.[10,40,41] Not only that, the ultrathin 2D could generate a higher density of surface atoms which function as active centers to boost photocatalytic processes as a result of the substantially enhanced specific surface area. The Brunauer–Emmett–Teller (BET) surface area of $BiVO_4$–A nanosheets were determined to be 144.37 $m^2 g^{-1}$, which is a striking 4.4-fold enhancement in comparison to $BiVO_4$–B (32. 47 $m^2 g^{-1}$). Figure S8, Supporting Information, features the N_2 adsorption–desorption isotherms of $BiVO_4$–A and $BiVO_4$–B samples. The ultrathin structure also synchronically reduces the transportation distance of electron–hole pairs formed in the core of $BiVO_4$ to the photocatalytic surface, effectively hampering the recombination of light-excited charge carriers.[22] These findings indubitably reveal that the rational design and hybridization of $BiVO_4$ with RP/BP with the coexistence of Z-scheme homo–heterojunction, surface disorder defects, and ultrathin 2D design are key contributors in achieving excellent CH_4 production.

To further consolidate the eminency and advantages of the ternary homo–heterojunction with dual Z-scheme system in comparison to binary heterojunction with single Z-scheme mechanism, CO_2 photoreduction was conducted for $BiVO_4$–Ov@RP, $BiVO_4$–A@RP, and $BiVO_4$–B@RP samples. In accordance with Figure 4a, the binary-component systems exhibited a much more inferior CH_4 production as opposed to the $BiVO_4$–Ov@RP/BP photocatalyst (14.52 μmol g^{-1}). The more superior photocatalytic performance demonstrated by the ternary dual Z-scheme system in comparison to the binary single Z-scheme mode could be justified by the presence of BP which endows a supplementary Ohmic junction for enhanced separation and transportation of charge carriers. The formation of two charge relay pathways at the interface of RP/BP and RP/$BiVO_4$–Ov indubitably improves the charge-carrier dynamics through encouraging the facile transfer of electrons by virtue of the more intense electric fields generated at the homo–heterojunction. These findings substantiate the merits of crafting a ternary dual Z-scheme photocatalytic system over binary single Z-scheme composites for the photoconversion of CO_2 to CH_4. To clarify the carbon source of CH_4 generated for the $BiVO_4$–Ov@RP/BP sample, isotope tracer analysis was undertaken by using $^{13}CO_2$ gas as the feedstock. Based on the inset of Figure 4a, $^{13}CH_4$ was generated from the isotope experiment, verifying that the carbon source for CH_4 production is not carbon-containing impurities. A comparison of photocatalytic CO_2-reduction performance for $BiVO_4$–Ov@RP/BP with other reported works is illustrated in Table S1, Supporting Information.[42–49] In this respect, $BiVO_4$–Ov@RP/BP displays much better CO_2-reduction performance than most $BiVO_4$-based photocatalysts. More importantly, exceptional photostability is demonstrated by the $BiVO_4$–Ov@RP/BP sample (Figure 4b), where the composite system maintained ≈91% of photocatalytic activity after three successive test cycles of CO_2 conversion. It is worth to note that the decline in photoactivity is a common occurrence for oxygen-defective materials as the dissociation of CO_2 molecules produces free oxygen atoms, that reoxidizes the surface with oxygen vacancies, resulting in the annihilation of oxygen defects.[36] The sample information and stability of the as-synthesized $BiVO_4$–Ov@RP/BP photocatalyst before and after three successive test cycles of photocatalytic CO_2 reduction were also investigated via XRD analysis as shown in Figure S9, Supporting Information. The results indicate no discernible change in diffraction peaks, suggesting that the as-developed composite photocatalyst possesses a relatively stable structure.

To unravel the mechanistic insights and charge transportation behaviors which led to the superlative CO_2-photoreduction performance of the $BiVO_4$–Ov@RP/BP hybrid photocatalyst, electrochemical impedance spectroscopy (EIS) Nyquist analysis was undertaken, and the Nyquist plots are depicted in Figure 4c. Based on the figure, $BiVO_4$–Ov@RP/BP exhibits a semicircle that is distinctly smaller and much more depressed than that of RP/BP, $BiVO_4$–A, $BiVO_4$–Ov, and $BiVO_4$–A@RP/BP. This suggests that the process of relaying electrons in the $BiVO_4$–Ov@RP/BP Z-scheme homo–heterojunction is a facile and smooth transportation process due to the intimate interfacial contact formed between RP and $BiVO_4$–Ov as well as RP and BP. This fortifies the presence of an internal electric field which is responsible for the vectorial transfer of electrons alongside the retardation of electron–hole pair recombination. In addition, the smaller arc radius observed for the Nyquist plot of $BiVO_4$–Ov@RP/BP entrenches that the sample possesses excellent electroconductivity due to the presence of surface oxygen-vacancy defects.[50] On the contrary, bare RP/BP, $BiVO_4$–A, and $BiVO_4$–Ov exhibit enlarged arc radius due to the absence of a secondary material that acts as a charge relay platform. In accordance with the Nyquist plot (Figure 4c), all the photocatalysts show a similar trend to their CO_2-reduction performances (Figure 4a). That said the charge-transfer impedance follows the descending order of RP/BP > $BiVO_4$–A > $BiVO_4$–Ov > $BiVO_4$–A@RP/BP > $BiVO_4$–Ov@RP/BP. Furthermore, results obtained from the EIS Nyquist analysis concur with the photoluminescence (PL) spectra in which the weaker emission peak of $BiVO_4$–Ov@RP/BP (Figure 4d) represents an enhanced separation and migration efficiency of electron–hole pairs as well as a concomitant improvement in charge-carrier lifespan attributed to the presence of oxygen vacancies endowing the trapping of electrons for suppressed recombination. Moreover, the large lateral dimension to thickness ratio of ultrathin 2D $BiVO_4$ nanosheets are well capable of shortening the migration distance of charge carriers, hence promoting a higher density of charges to participate in photocatalytic redox reactions prior to recombination. To study the fluorescence decay lifetime as well as the charge-carrier dynamics of the photocatalysts, time-resolved PL (TRPL) was employed as disclosed in Figure S10, Supporting Information. The standard bi-exponential model best describes the fluorescence decay profile as delineated by Equation (2) whereby B and τ represent the relative amplitude and lifetime for the individual component, respectively.

$$I(t) = A + B_1 \exp\left(\frac{-t}{\tau_1}\right) + B_2 \exp\left(\frac{-t}{\tau_2}\right) \quad (2)$$

The bi-exponential model converged and rendered a two-step fluorescence energy transfer in which the photocatalysts participated in both fast τ_1 (near band-edge emission) and slow τ_2 (trap state emission) energy-transfer processes. Intriguingly, The $BiVO_4$–Ov sample was revealed to exhibit the longest decay lifetime of 1.0 ns, which is greater in comparison to the average decay lifetime of $BiVO_4$–A (0.68 ns) and RP/BP (0.45 ns). The

prolonged average decay lifetime of $BiVO_4$–Ov as opposed to $BiVO_4$–A corroborates the effective impediment of charge-carrier recombination attributing to the incorporation of oxygen vacancies in $BiVO_4$ that serve as electron reservoir. In contrast, the average decay lifetime of $BiVO_4$–Ov@RP/BP is significantly reduced to 0.35 ns, implying the enhanced charge migration behavior and expedited electron transfer separating the emissive state across the internal electric field of the Z-scheme system.

First principles calculations were employed to further unravel the effects of oxygen-vacancy defects incorporation on the electronic properties and structure of ultrathin 2D $BiVO_4$–Ov nanosheets. We determined the defect formation energies as summarized in Table S2, Supporting Information, for the $BiVO_4$–lattice where four sites were investigated to dictate the most favorable site for oxygen atom removal; they are surface oxygen atoms coordinated to V (O1), surface oxygen atoms coordinated to Bi (O_2), bulk oxygen atoms coordinated to Bi (O_3), and bulk oxygen atoms coordinated to V (O_4). Intriguingly, the formation of oxygen-vacancy defect at O_2 (circled in blue as shown in **Figure 5**a) rendered the lowest formation energy, i.e., −3.37 eV, revealing it to be the most probable site for defect (energetically favorable) in $BiVO_4$ since a more negative energy of formation suggests the thermodynamic feasibility and stability of the configuration. Henceforth, O_2 configuration was adopted as the model of concept for $BiVO_4$–Ov, and its optoelectronic behaviors and charge dynamics were explored to unearth the significance of defect engineering via oxygen-vacancy incorporation in improving photocatalytic performance.

The partial density of states (PDOS) of $BiVO_4$ integrated with and without oxygen vacancies can be observed in Figure 5b. It is noted that both pristine $BiVO_4$ and $BiVO_4$–Ov nanosheets share similar PDOS profile in which their VB is greatly dominated by O 2p orbital whereas their CB is contributed by O 2p, Bi 6p, and V 3*d* orbitals. The integration of oxygen vacancies witnesses the downshift of CB energy level, indicating bandgap narrowing, and suggests that the oxygen vacancies can efficaciously augment the visible-light responsivity of $BiVO_4$–Ov. These alterations favorably elevate the photogeneration and photoexcitation of electrons and holes for participation in reduction and oxidation reactions, respectively. Figure 5c delineates the charge density spatial distribution at the Fermi level. In accordance with the figure, majority of positive charge carriers (yellow regions) are concentrated around the oxygen-vacancy sites whereas negative charge carriers (dark blue regions) are localized around surrounding neighboring atoms. The electron-depleted oxygen-vacancy defect states in $BiVO_4$–Ov allow the trapping of photogenerated electrons upon the illumination of visible light. This corroborates the claim that oxygen vacancies facilitate the accumulation of electrons, which lead to the creation of an inner electric zone that is beneficial for the formation of depletion layers at the interface of $BiVO_4$–OV@RP/BP.[16] Hence, effective migration of electrons and holes can occur, leading to the construction of cascade electron flow, which represents the Z-scheme configuration.

3. Conclusion

In summary, we have successfully developed and coupled ultrathin 2D $BiVO_4$ with RP/BP with the coexistence of oxygen-vacancy defects on $BiVO_4$ and dual Z-scheme homo–heterointerface. The as-synthesized $BiVO_4$ nanosheets possess an average thickness of less than 5 nm and surface oxygen-vacancy defects. These exemplary features bestow $BiVO_4$–Ov nanosheets with superior optoelectronic properties and photooxidation performance such that when it is amalgamated with RP/BP, the CH_4 evolution rate reached 14.52 μmol g^{-1}. In stark contrast, RP/BP, $BiVO_4$–Ov, and $BiVO_4$–A displayed unsatisfactory CO_2-reduction performance as no CH_4 was detected for these samples. With the ingenious combination of defect engineering and ultrathin 2D material design in $BiVO_4$ and its subsequent hybridization with mixed-phase RP/BP for the formation of dual Z-scheme homo–heterojunction, the isolation and life span of electron–hole pairs are substantially enhanced. In particular, surface oxygen-vacancy defects present in $BiVO_4$ temporarily occupy the electrons to delay exciton recombination whereas its ultrathin 2D structure

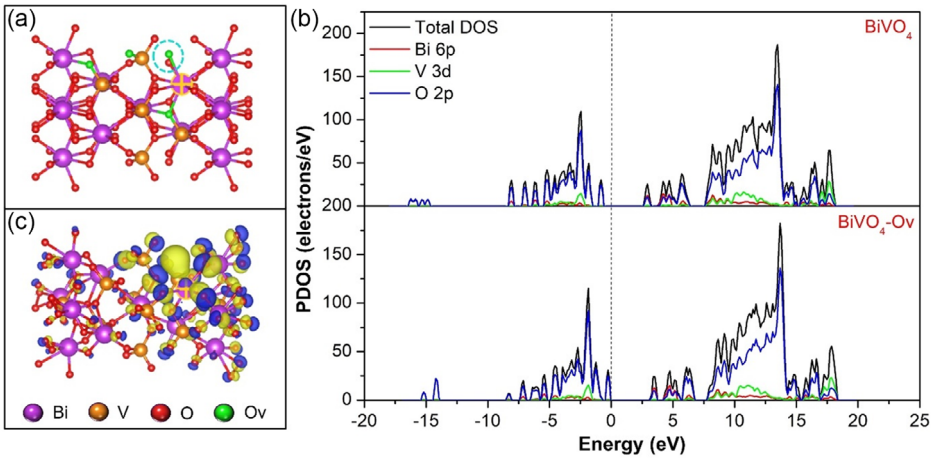

Figure 5. a) Schematic view of the optimized structure for the four considered configurations of oxygen-vacancy defect sites (green ball-and-stick) for $BiVO_4$. Formation of oxygen-vacancy defect at O_2 (circled in blue) is the most energetically favorable site. b) Partial density of states (PDOS) of $BiVO_4$ and $BiVO_4$–Ov. Fermi level is resembled by the dashed line. c) Charge density differences for the most preferable oxygen-vacancy defect site for $BiVO_4$–Ov. The yellow and dark blue regions represent depletion and accumulation of electrons, respectively.

effectively amplifies the contact surface area while minimizing the charge migration distance from the core to the surface of the photocatalyst. Cooperating synergistically with the intense internal electric field at the $BiVO_4$–Ov@RP/BP homo–heterointerface which warrants a dominant steering force for Z-scheme electron transportation, the presence of dual space-charged regions and lower resistance to charge-transfer encourage the smooth transportation of electron–hole pairs to the surface of the photocatalysts to augment their participation in photocatalytic reactions. As a whole, the development of $BiVO_4$–Ov@RP/BP in this work affords new inspiration for the rational steering of charge transfer and modulation of catalytic active sites to realize efficacious CO_2-reduction activity.

4. Experimental Section

Materials: RP powder (≥97.0%, Sigma Aldrich), ethylenediamine (EDA) (≥98.0%, Nacalai Tesque), ethanol (C_2H_5OH) (Grade AR 96.0%, Friendemann Schmidt Chemical), bismuth (III) nitrate pentahydrate powder ($Bi(NO_3)_3 \cdot 5H_2O$) (≥98.0%, Sigma Aldrich), ammonium metavanadate (NH_4VO_3) (≥99.0%, Merck), oleyamine (OLA) (≥70.0%, Sigma Aldrich), oleic acid (OA) (≥90.0%, Sigma Aldrich), 1-octadecene (ODE) (≥90.0%, Sigma Aldrich), hexane (C_6H_{14}) (≥98.0%, Sigma Aldrich), nitric acid (HNO_3) (≥65.0%, Merck), and dimethyl sulfoxide solution (DMSO) (≥99.9%, Macron Fine Chemicals) were of analytical grade and utilized as received without further purification. Throughout the entire experiment, deionized H_2O with a resistivity ≥18.0 MΩ cm was utilized.

Purification of RP: Purification of RP photocatalysts was first undertaken via a facile hydrothermal treatment route to eliminate the oxide layer on the surface of the material. Typically, 3.0 g of commercial bulk RP was added into 80 mL of deionized H_2O and vigorously stirred. The dissolved mixture was subsequently loaded and sealed in a Teflon-lined stainless autoclave. The autoclave reactor was then heated to 200 °C in a muffle furnace and maintained for 12 h. After cooling down to room temperature, the products were collected and washed with ethanol and deionized H_2O three times, respectively. Finally, the products were left to dry overnight at 60 °C in a vacuum oven.

Synthesis of Mixed-Phase RP/BP Homojunction Photocatalyst: By using EDA as the reaction solvent and purified RP as the feedstock, a simple one-step wet-chemistry approach was employed to fabricate the mixed-phase RP/BP homojunction. In a typical procedure, 60 mL of EDA solution was used to dissolve 1.80 g of purified RP by vigorously stirring the mixture for 30 min. Thereafter, the solution consisting of RP uniformly dispersed in EDA solvent was poured into a Teflon-lined stainless autoclave. The mixture was then heated to 165 °C in a muffle furnace and maintained for 16 h. After cooling down to room temperature, the products were collected and washed with ethanol and deionized H_2O three times, respectively. Finally, the products were left to dry overnight at 60 °C in a vacuum oven.

Synthesis of Oxygen-Defective Ultrathin BiVO4 Nanosheets: In a typical synthesis, 0.5 mmol of $Bi(NO_3)_3 \cdot 5H_2O$ was added to a solution comprising 1 mL of OA, 1 mL of OLA, and 10 mL of ODE, and the mixture was poured into a three-neck flask. The solution in the three-neck flask was degassed by purging nitrogen (N_2) for 30 min under vigorous stirring and then heated to 170 °C using a heating mantle equipped with a magnetic stirrer. In another beaker, a mixture of 10 mL of deionized H_2O and 2 mL of HNO_3 was prepared and 1 mmol of NH_4VO_3 was later added and dissolved in the H_2O/HNO_3 mixture until a bright yellow solution was obtained. The aqueous NH_4VO_3 solution was then carefully injected into the three-neck flask comprising dissolved $Bi(NO_3)_3 \cdot 5H_2O$ in OA/OLA/ODE mixture. Under inert N_2 environment, the reaction temperature was adjusted to 100 °C and maintained for 30 min. The mixture was left to cool naturally upon the termination of the heat source after 30 min. The products in the three-neck flask were then poured into a mixture of ethanol and hexane to stratify the solution and the subjacent aqueous solution was removed. The remaining solution which contained the ultrathin $BiVO_4$–Ov nanosheets was centrifuged at 7500 rpm for 10 min. A mixture of ethanol and hexane was used to wash the precipitates five times. The final precipitates were collected and dried overnight. It must be emphasized that the addition of HNO_3 was indispensable in dissolving NH_4VO_3 and introducing oxygen vacancies into the $BiVO_4$ nanosheets owing to the presence of hydroxyl groups. When heated to a temperature of 100 °C in the presence of OA, OLA, and ODE, VO_3^- or VO_4^{3-} was postulated to be present as VO_2^+ in HNO_3 aqueous solution, and the reduction of VO_2^+ by OA and OLA eventually led to the formation of oxygen vacancies (V^{4+}). Apart from that, HNO_3 also played a pivotal role in constructing the ultrathin 2D structure as the hydroxyl groups present established a highly acidic environment that decreased the surface energy of the $BiVO_4$ to encourage the formation of 2D geometry. It is therefore believed that the ultrathin $BiVO_4$ nanosheets that were exposed in a solution of highly concentrated HNO_3 possessed a much more stable structure and lowest surface free energy.[20]

Synthesis of Ultrathin BiVO4 Nanosheets without Oxygen Vacancies and Bulk BiVO4: To corroborate the existence of oxygen vacancies in $BiVO_4$–Ov nanosheets and study their effects on optoelectronic properties and photocatalytic reactions, $BiVO_4$ nanosheets without oxygen vacancies were also prepared. In detail, the ultrathin $BiVO_4$–Ov samples underwent thermal treatment via annealing in air at 500 °C. By virtue of the passivation impacts of oxygen, the number of oxygen-vacancy defects would be substantially minimized. The annealed sample is referred to as $BiVO_4$–A. Bulk $BiVO_4$ ($BiVO_4$–B) was also prepared. Specifically, 20 mmol of $Bi(NO_3)_3 \cdot 5H_2O$ and 20 mmol of NH_4VO_3 were dissolved in 80 mL of deionized H_2O under 1 h of continuous stirring. Thereafter, the solution was poured into a Teflon-lined stainless autoclave. The mixture was then heated to 180 °C in a muffle furnace and maintained for 6 h. After cooling down to room temperature, the products were collected and washed with ethanol and deionized H_2O three times, respectively. Finally, the products were left to dry overnight at 60 °C in a vacuum oven.

Preparation of Ultrathin $BiVO_4$–Ov@RP/BP Homo–Heterojunction Photocatalyst: The $BiVO_4$–Ov@RP/BP samples were fabricated by a facile sonochemical strategy. In detail, 0.1 g of RP/BP and 0.1 g of $BiVO_4$–Ov were added and dispersed in 100 mL of DMSO solution. The RP/BP and $BiVO_4$ dispersion was stirred continuously for 2 h and subsequently ultrasonicated for another 2 h. High speed centrifugation (7500 rpm, 30 min) was employed to collect the products from the dispersion. The products were later washed with ethanol and deionized H_2O three times, respectively. Finally, the $BiVO_4$–Ov@RP/BP products were dried overnight at 60 °C in a vacuum oven. Similar technique was used to prepare $BiVO_4$–A@RP/BP and $BiVO_4$–B@RP/BP.

Materials Characterization: The structural characteristics, morphology, and elemental composition of the photocatalytic samples were observed and assessed using a Hitachi SU8010 FESEM integrated with EDX. In contrast, HRTEM images were acquired using TECNAI G2 F20 TEM. The topography and thickness of $BiVO_4$–Ov nanosheets were obtained using Bruker Multimode 8 AFM. The XPS analysis was conducted using a Phoibos 100 spectrometer (SPECS, Germany), which employs a monochromatic Al–Kα X-Ray source. A charge correction before deconvolution with reference to the C–C peak possessing a binding energy of 284.60 eV from the C 1s spectra was applied to the binding energies obtained for all the samples. UPS analysis was undertaken using Nexsa G2 Surface Analysis System (Thermo Fisher Scientific) by using vacuum UV radiation for the induction of photoelectric effects. The emission of photons by helium gas possessed an energy of 21.2 eV (He I). The powder XRD patterns and crystallographic behaviors of the developed materials were analyzed using a Bruker D8 Discover X-Ray diffractometer at a scanning rate of 0.02 s^{-1} with nickel (Ni)-filtered copper (Cu) Kα radiation. To verify the presence of oxygen-vacancy defects in $BiVO_4$–Ov nanosheets, ESR spectrometer (JEOL, JES-FA200) was employed. By utilizing a Micromeritics 3Flex instrument, the BET surface area of the photocatalysts was attained via the adsorption of N_2 at a temperature of 77 K. In addition, Agilent Cary 100 UV–Vis spectrophotometer equipped with an integrated sphere was utilized to measure and analyze the optical absorption spectra of all samples for the wavelength ranging from 200 to 800 nm, with $BaSO_4$ as the reflectance standard. PL) measurements were obtained with the assistance of a LS 55, Perkin Elmer fluorescence spectrophotometer, at an

excitation wavelength of 300 nm. The TRPL properties of the photocatalysts were assessed using HORIBA DeltraPro-DD time-resolved spectrofluorometer at an excitation wavelength of 317 nm.

Electrochemical Analysis: The photoelectrochemical measurements of the developed photocatalysts namely Mott–Schottky and Nyquist analysis were undertaken using a CHI 6005 E electrochemical workstation equipped with a standard three-electrode cell. In the electrochemical system, Pt rod functioned as the counter electrode whereas Ag/AgCl saturated with 3 M KCl served as the reference electrode. The system also comprised a working electrode and an electrolyte (0.5 M Na_2SO_4). To prepare the working electrode, photocatalyst powder was first suspended in ethanol/Nafion (4.90 mL: 0.10 mL) solution and subsequently spray-coated onto an fluorine-doped tin oxide (FTO) glass slide with 1 cm^2 of active area. Mott–Schottky analysis was conducted at a frequency of 100 Hz within a range of −2.0–0.50 V and a potential step of 50.0 mV. Conversely, at an applied potential of 0.20 V (vs. Ag/AgCl), the EIS measurements were recorded at an AC sinusoidal perturbation signal of 10.0 mV and a frequency of 10^{-2}–10^{6} Hz.

Evaluation of Photocatalytic Activities: The photocatalytic performances of the developed photocatalysts were evaluated via the conversion of CO_2 to CH_4. The CO_2-photoreduction experiment was undertaken at ambient conditions in a photocatalysis rig which featured a custom-made, continuous gas flow reactor. A 500 W xenon arc lamp (CHF-XM-500 W) equipped with UV cutoff filter ($\lambda > 400$ nm) was used as the visible-light source. For the setup of the CO_2 conversion experiment, photocatalyst powder was coated onto two glass rods which were subsequently placed into their respective quartz columns prior to the start of the CO_2-photoreduction experiment. The quartz columns were situated in an enclosed black box to eliminate external light source interferences. The columns were firmly hitched into the quartz column holder to ascertain that they remained affixed throughout the entire photoconversion experiment. Each end of the quartz column was then attached with individual piping. To provide CO_2–H_2O gas mixture, high purity CO_2 gas (99.999 %) was bubbled through liquid H_2O and channeled into the photocatalysis rig as the reactant gas. Before starting the photocatalytic reduction experiment, the system was purged with CO_2–H_2O gas mixture at a flow rate of 50 mL min^{-1} for 30 min to eliminate contaminants from the quartz columns and to ensure the achievement of adsorption–desorption equilibrium on the photocatalyst surface. After purging, the CO_2–H_2O gas mixture flow rate was adjusted to 5 mL min^{-1} for 6 h under visible-light irradiation. A gas chromatography (Agilent 7820 A GC) using helium as a carrier gas and equipped with flame-ionized detector and thermal conductivity detector was employed to quantify and examine the product gas components at hourly intervals. The total CH_4 yield was calculated using Equation (3).

$$\text{Yield}\ (\mu\text{mol g}^{-1}) = \frac{\text{Moles of product formed}\ (\mu\text{mol})}{\text{Mass of photocatalyst used}\ (\text{g})} \quad (3)$$

To attest the carbon source of CH_4 gas generated, isotope experiment was undertaken for the $BiVO_4$–Ov@RP/BP sample using $^{13}CO_2$ gas as the feedstock and the products were analyzed using GC mass spectrometry (Agilent 7890 A and 5975 C).

DFT Calculation: To obtain the $BiVO_4$ structure in the present study, a vacuum of 15 Å was added in the *z*-direction of a bulk supercell (115-atom model).[51] The $BiVO_{4-x}$ model was generated by removing the surface O atoms coordinated to V (O_1) and Bi (O_2) and bulk O atoms coordinated to Bi (O_3) and V (O_4) with coordination number of two and three, resulting in a total of four $BiVO_{4-x}$ slabs models. The spin-polarized DFT calculations were carried out in the Vienna ab initio simulation package (VASP) suite of programs (v5.4.4).[52] The electron exchange–correlation interactions were described based on the Perdew–Burke–Ernzerhof of the generalized gradient approximation functional.[53] The projector-augmented-wave pseudopotentials for each atomic species specified in the calculation were determined by VASP.[54] The long-range van der Waals interactions were included based on Grimme's DFT-D3 method.[55] An energy cutoff of 500 eV was adopted for the plane-wave basis set. All ions were allowed to relax until the residual Hellmann–Feynman forces were less than 0.01 eV $Å^{-1}$ and the electronic self-consistency was converged to below 10^{-5} eV. Monkhorst–Pack scheme for the reciprocal space *k*-point meshes of $3 \times 3 \times 2$ was used to sample the Brillouin zone.[56]

Supporting Information

Supporting Information is available from the Wiley Online Library or from the author.

Acknowledgements

This work was funded by the Ministry of Higher Education (MOHE) Malaysia under the Fundamental Research Grant Scheme (FRGS) (ref no. FRGS/1/2019/TK02/MUSM/01/1).

Open access publishing facilitated by Monash University, as part of the Wiley - Monash University agreement via the Council of Australian University Librarians.

Conflict of Interest

The authors declare no conflict of interest.

Data Availability Statement

The data that support the findings of this study are available from the corresponding author upon reasonable request.

Keywords

oxygen-vacancy defects, photocatalytic CO_2 reduction, ultrathin 2D photocatalysts, Z-schemes

Received: March 8, 2023
Revised: June 11, 2023
Published online: August 8, 2023

[1] Carbon Dioxide Now More than 50% Higher than Pre-Industrial Levels, National Oceanic and Atmospheric Administration, https://www.noaa.gov/news-release/carbon-dioxide-now-more-than-50-higher-than-pre-industrial-levels (accessed: June 2023).
[2] D. Gerten, R. Adrian, *Sci. World J.* **2002**, *2*, 586.
[3] C. M. Fung, J. Y. Tang, L. L. Tan, A. R. Mohamed, S. P. Chai, *Mater. Today Sustain.* **2020**, *9*, 100037.
[4] L. Liu, M. Li, F. Chen, H. Huang, *Small Struct.* **2023**, *4*, 2200188.
[5] Y. Zhao, S. Zhang, R. Shi, G. I. N. Waterhouse, J. Tang, T. Zhang, *Mater. Today* **2020**, *34*, 78.
[6] W. Yang, X. Zhang, Y. Xie, *Nano Today* **2016**, *11*, 793.
[7] J. Di, J. Xiong, H. Li, Z. Liu, *Adv. Mater.* **2018**, *30*, 1704548.
[8] A. Malathi, J. Madhavan, M. Ashokkumar, P. Arunachalam, *Appl. Catal. A Gen.* **2018**, *555*, 47.
[9] P. Chen, N. Li, X. Chen, W.-J. Ong, X. Zhao, *2D Mater.* **2018**, *5*, 014002.
[10] H. Li, J. Li, Z. Ai, F. Jia, L. Zhang, *Angew. Chem. Int. Ed.* **2018**, *57*, 122.
[11] F. Chen, Y. Zhang, H. Huang, *Chinese Chem. Lett.* **2023**, *34*, 107523.
[12] Y. C. Zhang, Z. Li, L. Zhang, L. Pan, X. Zhang, L. Wang, Fazal-e-Aleem, J. J. Zou, *Appl. Catal. B Environ.* **2018**, *224*, 101.
[13] G. Q. Zhao, J. Hu, X. Long, J. Zou, J. G. Yu, F. P. Jiao, *Small* **2021**, *17*, 2102155.

[14] A. Hezam, K. Namratha, Q. A. Drmosh, D. Ponnamma, J. Wang, S. Prasad, M. Ahamed, C. Cheng, K. Byrappa, *ACS Appl. Nano Mater.* **2020**, *3*, 138.
[15] H. Yu, F. Chen, X. Li, H. Huang, Q. Zhang, S. Su, K. Wang, E. Mao, B. Mei, G. Mul, T. Ma, Y. Zhang, *Nat. Commun.* **2021**, *12*, 4594.
[16] S. Mansingh, D. Kandi, K. K. Das, K. Parida, *ACS Omega* **2020**, *5*, 9789.
[17] C. M. Fung, C. C. Er, L. L. Tan, A. R. Mohamed, S. P. Chai, *Chem. Rev.* **2021**, *122*, 3879.
[18] C.-M. Fung, B.-J. Ng, C.-C. Er, X. Y. Kong, L.-L. Tan, A. R. Mohamed, *ACS Appl. Energy Mater.* **2022**, *5*, 15257.
[19] Y. Liu, H. Wang, X. Yuan, Y. Wu, H. Wang, Y. Z. Tan, J. W. Chew, *Chem Catal.* **2021**, *1*, 44.
[20] D. Yao, C. Dong, Q. Bing, Y. Liu, F. Qu, M. Yang, B. Liu, B. Yang, H. Zhang, *ACS Appl. Mater. Interfaces* **2019**, *11*, 23495.
[21] H. L. Tan, X. Wen, R. Amal, Y. H. Ng, *J. Phys. Chem. Lett.* **2016**, *7*, 1400.
[22] C. Dong, S. Lu, S. Yao, R. Ge, Z. Wang, Z. Wang, P. An, Y. Liu, B. Yang, H. Zhang, *ACS Catal.* **2018**, *8*, 8649.
[23] W. Zhao, Z. Xue, J. Wang, J. Jiang, X. Zhao, T. Mu, *ACS Appl. Mater. Interfaces* **2015**, *7*, 27608.
[24] M. Qiu, D. Wang, W. Liang, L. Liu, Y. Zhang, X. Chen, D. K. Sang, C. Xing, Z. Li, B. Dong, F. Xing, D. Fan, S. Bao, H. Zhang, Y. Cao, *Proc. Natl. Acad. Sci. U. S. A* **2018**, *115*, 501.
[25] H. Wang, D. Yong, S. Chen, S. Jiang, X. Zhang, W. Shao, Q. Zhang, W. Yan, B. Pan, Y. Xie, *J. Am. Chem. Soc.* **2018**, *140*, 1760.
[26] T. Qin, X. Zhang, D. Wang, T. Deng, H. Wang, X. Liu, X. Shi, Z. Li, H. Chen, X. Meng, W. Zhang, W. Zheng, *ACS Appl. Mater. Interfaces* **2019**, *11*, 2103.
[27] Q. Wang, B. Li, P. Zhang, W. Zhang, X. Hu, X. Li, *RSC Adv.* **2020**, *10*, 27538.
[28] H. Li, H. Gong, Z. Jin, *Appl. Catal. B Environ.* **2022**, *307*, 121166.
[29] X. Zhu, T. Zhang, D. Jiang, H. Duan, Z. Sun, M. Zhang, H. Jin, R. Guan, Y. Liu, M. Chen, H. Ji, P. Du, W. Yan, S. Wei, Y. Lu, S. Yang, *Nat. Commun.* **2018**, *9*, 1191.
[30] W. Ding, D. Liu, J. Liu, J. Zhang, *Chinese J. Chem.* **2020**, *38*, 1832.
[31] G. Li, H. Zhang, L. Meng, Z. Sun, Z. Chen, X. Huang, Y. Qin, *Sci. Bull.* **2020**, *65*, 1650.
[32] S. N. F. M. Nasir, H. Ullah, M. Ebadi, A. A. Tahir, J. S. Sagu, M. A. M. Teridi, *J. Phys. Chem. C* **2017**, *121*, 6218.
[33] Y. H. Chew, J. Y. Tang, L. J. Tan, B. W. J. Choi, L. L. Tan, S. P. Chai, *Chem. Commun.* **2019**, *55*, 6265.
[34] A. Thøgersen, M. Syre, B. Retterstol Olaisen, S. Diplas, *J. Appl. Phys.* **2013**, *113*, 044307.
[35] B. Ng, L. K. Putri, X. Y. Kong, Y. W. Teh, P. Pasbakhsh, S. Chai, *Adv. Sci.* **2020**, *7*, 1903171.
[36] X. Y. Kong, W. Q. Lee, A. R. Mohamed, S. P. Chai, *Chem. Eng. J* **2019**, *372*, 1183.
[37] J. Y. Tang, X. Y. Kong, B. J. Ng, Y. H. Chew, A. R. Mohamed, S. P. Chai, *Catal. Sci. Technol.* **2019**, *9*, 2335.
[38] S. Wang, X. Han, Y. Zhang, N. Tian, T. Ma, H. Huang, *Small Struct.* **2021**, *2*, 2000061.
[39] Y. Huang, W. Wang, Y. Zhang, J. Cao, R. Huang, X. Wang, *Nov. Nanomater. Biomed. Environ. Energy Appl.* **2019**, 299.
[40] J. Di, C. Chen, S. Z. Yang, M. Ji, C. Yan, K. Gu, J. Xia, H. Li, S. Li, Z. Liu, *J. Mater. Chem. A* **2017**, *5*, 14144.
[41] X. Jiao, Z. Chen, X. Li, Y. Sun, S. Gao, W. Yan, C. Wang, Q. Zhang, Y. Lin, Y. Luo, Y. Xie, *J. Am. Chem. Soc.* **2017**, *139*, 7586.
[42] Q. Bi, K. Hu, J. Chen, Y. Zhang, M. S. Riaz, J. Xu, Y. Han, F. Huang, *Appl. Catal. B Environ.* **2021**, *295*, 120211.
[43] C. Han, J. Li, Z. Ma, H. Xie, G. I. N. Waterhouse, L. Ye, T. Zhang, *Sci. China Mater.* **2018**, *61*, 1159.
[44] R. Niu, Q. Liu, B. Huang, Z. Liu, W. Zhang, Z. Peng, Z. Wang, Y. Yang, Z. Gu, J. Li, *Appl. Catal. B Environ.* **2022**, *137*, 121727.
[45] R. A. Rather, M. Khan, I. M. C. Lo, *J. Catal.* **2018**, *366*, 28.
[46] K. Hu, Z. Li, S. Chen, J. Bian, Y. Qu, J. Tang, L. Jing, *Part. Part. Syst. Charact.* **2018**, *35*, 1700320.
[47] X. Yue, L. Cheng, J. Fan, Q. Xiang, *Appl. Catal. B Environ.* **2022**, *304*, 120979.
[48] Z. H. Wei, Y. F. Wang, Y. Y. Li, L. Zhang, H. C. Yao, Z. J. Li, *J. CO2 Util.* **2018**, *28*, 15.
[49] Q. Han, L. Li, W. Gao, Y. Shen, L. Wang, Y. Zhang, X. Wang, Q. Shen, Y. Xiong, Y. Zhou, Z. Zou, *ACS Appl. Mater. Interfaces* **2021**, *13*, 15092.
[50] Y. Shin, K. Y. Doh, S. H. Kim, J. H. Lee, H. Bae, S. J. Song, D. Lee, *J. Mater. Chem. A* **2020**, *8*, 4784.
[51] C. C. Er, J. Y. Tang, C. M. Fung, L. L. Tan, N. V. Medhekar, S. P. Chai, *J. Phys. Chem. C* **2021**, *125*, 23021.
[52] G. Kresse, J. Furthmüller, *Phys. Rev. B Condens. Matter Mater. Phys.* **1996**, *54*, 11169.
[53] J. P. Perdew, K. Burke, M. Ernzerhof, *Phys. Rev. Lett.* **1996**, *77*, 3865.
[54] D. Joubert, *Phys. Rev. B Condens. Matter Mater. Phys.* **1999**, *59*, 1758.
[55] S. Grimme, J. Antony, S. Ehrlich, H. Krieg, *J. Chem. Phys.* **2010**, *132*, 154104.
[56] H. J. Monkhorst, J. D. Pack, *Phys. Rev. B* **1976**, *13*, 5188.